PAPER

Check for updates

Engineered etching and laser treatment of porous silicon for enhanced sensitivity and speed of Pt/n-PSi/Pt UV photodetectors

Asad A. Thahe,[*a] Ali Dahi,[b] Motahher A. Qaeed,[c] Omar F. Farhat,[d] Hazri Bakhtiar[e] and Nageh K. Allam [ID] [*f]

Silicon-based photodetectors offer notable advantages in cost, performance, and reliability. However, while nanoscale silicon (porous silicon, PSi) effectively emits visible light, it remains inefficient as an indirect-bandgap semiconductor. To improve its optoelectronic properties, coupling silicon with a wide-bandgap semiconductor is a promising strategy. In this study, nanoporous silicon (n-PSi) films were fabricated from an n-type Si (111) wafer using optimized photoelectrochemical etching (PECE). These films were then irradiated with Q-switched Nd:YAG laser pulses (3, 5, 10, and 20 pulses) at a fixed wavelength of 1068 nm, with pulse durations ranging from 3 to 20 ns and a constant repetition rate of 10 Hz. The structural, morphological, and optical properties of both as-prepared and laser-annealed n-PSi samples were characterized using various analytical techniques. Among the laser-treated samples, n-PSi subjected to three laser pulses exhibited the highest crystallinity and largest crystallite size ($\sim$87.02 nm). This optimized sample was selected for fabricating a Pt/n-PSi/Pt metal–semiconductor–metal (MSM) ultraviolet (UV) photodetector. The photoluminescence spectra of the fabricated devices revealed strong near-band-edge (NBE) emission, with a violet band centered around 523 nm, corresponding to a bandgap energy of 2.36 eV. The $I–V$ characteristics of the MSM UV photodetectors were analyzed under dark conditions and 380 nm UV illumination. The device demonstrated high photosensitivity (951.28), excellent responsivity (2.01 A W^{-1}), and fast response (0.44 s) and recovery (0.48 s) times, outperforming conventional photodetectors. This approach provides a viable pathway for tuning nanomaterials with tailored properties for high-performance nanodevices. The fabricated MSM UV photodetectors show great potential for next-generation optoelectronic applications.

1. Introduction

Silicon is a fundamental material in electronics due to its abundance, excellent functional properties, and high-quality fabrication potential.[1] However, its high refractive index ($n = 3.4$ at 550 nm) in the 300–1100 nm wavelength range leads to significant optical losses,[2] necessitating surface enhancement techniques. One effective approach is the formation of nanoporous silicon (PSi), which increases surface area and enhances efficiency, making it highly promising for optoelectronic applications.

aDepartment of Medical Physics, College of Applied Science, University of Fallujah, Fallujah, Iraq. E-mail: asaad.thahe@uofallujah.edu.iq

bCollege of Pharmacy, University of Al Maarif, Al Anbar 31001, Iraq

cDepartment of Physical Sciences, Faculty of Science, University of Jeddah, Saudi Arabia

dPhysics Department, Faculty of Science, Alasmarya Islamic University, Zliten, Libya

eLaser Center, Universiti Teknologi Malaysia, Skudai, Johor, 81310, Malaysia

fEnergy Masteries Laboratory, Physics Department, School of Sciences and Engineering, The American University in Cairo, New Cairo 11835, Egypt. E-mail: nageh.allam@aucegypt.edu

The unique morphology of PSi has enabled advancements in Si-based photodetectors, which offer advantages in cost, performance, and reliability. However, nanoscale PSi remains inefficient as a direct-bandgap semiconductor. While its photoluminescence efficiency can reach 23%, its electroluminescence efficiency is much lower, around 1%.[3,4] Additionally, silicon ultraviolet photodetectors (UV PDs) face several challenges, including reduced photoresponse under high-energy radiation, sensitivity to visible light, and passivation layer effects that impact deep-UV quantum efficiency.[5] To overcome these limitations, coupling silicon with wide-bandgap semiconductors has been explored as a strategy to enhance photodetector performance.

Previous studies, such as those by Ueamanapong *et al.*,[6,7] demonstrated that Pt-doped Si-based metal–semiconductor–metal (MSM) photodetectors can detect 365 nm light. However, the efficiency of these devices largely depends on the quality of the fabricated PSi films, necessitating precise growth control. Electrochemical etching is a well-suited method for synthesizing high-quality n-type PSi (n-PSi) with tunable porosity, morphology, and optoelectronic properties.[8] Optimizing

photoelectrochemical etching (PECE) parameters—such as etching duration and current density—significantly influences the structural and optical characteristics of PSi.[9,10] Moreover, studies suggest that coating PSi with n-type semiconductor materials further improves crystallinity and charge transport properties.[10,11]

Despite ongoing efforts to enhance PSi-based photodetectors, achieving ideal fabrication conditions remains challenging. The demand for n-PSi in UV PD applications is growing across various fields, including medicine, manufacturing, and technology.[11–13] While previous research has examined the electrical and photoresponse properties of Nd:YAG-annealed Pt/n-PSi/Pt photodetectors at different laser energies,[1] the impact of Nd:YAG laser pulses on their photophysical performance has not been fully explored.

This study investigates the effect of pulsed Nd:YAG laser irradiation on the performance of Pt/n-PSi/Pt photodetectors fabricated *via* electrochemical etching. Additionally, it examines how laser fluence influences the morphological, structural, and optical properties of the PSi layer, providing critical insights into optimizing PSi for high-performance UV photodetection.

2. Experimental section

2.1. Photoelectrochemical etching cell (PECE)

Fig. 1 illustrates the design and construction of the PECE cell used for depositing the PSi layer on an n-type Si wafer. The cell is made of Teflon (polytetrafluoroethylene) and features a 1 cm diameter circular aperture at the bottom, sealed by the synthesized Si specimen. During the etching process, a 50 W visible lamp positioned above the cell illuminates the silicon sample, with Si serving as the anode and platinum (Pt) wire as the cathode.

2.2. Nd-YAG laser annealing

The optimal n-PSi sample, prepared at a current density of 45 mA cm^{-2}, was selected for Nd:YAG laser annealing with varying pulse numbers (3, 5, 10, and 20). A Q-switched Nd:YAG laser with a wavelength of 1064 nm and a pulse duration of 10 ns (Fig. 2) was used for the annealing process. The beam size was initially determined using burn paper, and the resulting burn

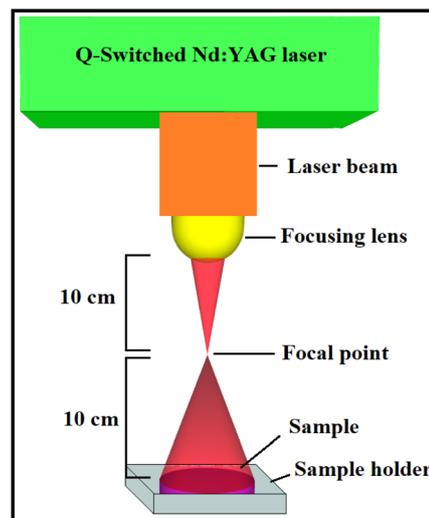Fig. 1 Graphical representation of the PECE cell used to generate n-PSi samples.

Fig. 2 Schematic presentation for experimental setup of the laser annealing process.

mark was measured to estimate the beam area, which was found to be approximately 0.785 cm^2. The laser beam was focused vertically onto the target film using a lens with a focal length of 10 cm. To measure the laser power, the sensor head of an Ophir NOVA energy meter (PE50 sensor head) was positioned 10 cm beyond the focal point of the focusing lens. The energy density at the target was calculated to be approximately 40 mJ cm^{-2}, with energy of 31.42 mJ at the target position. Fig. 2 illustrates the schematic arrangement of the setup. The effects of laser annealing on the structural, morphological, and photoluminescence (PL) properties of n-PSi were analyzed to identify the optimal sample for MSM UV photodiode fabrication. The primary objective of laser annealing was to enhance the photodiode's performance, with the n-PSi film annealed using 3 pulses identified as the optimal sample. The laser-irradiated area was calculated using eqn (1) below.

$$A = \pi r^2 \qquad (1)$$

where A represents the laser irradiated area and r symbolizes the radius (0.5 cm). The energy density (E_d) was calculated using eqn (2):

$$E_d = \frac{E}{A} \qquad (2)$$

where E_d signifies energy density (40 mJ cm^{-2}), E represents energy at the target position (31.42 mJ), and A denotes the laser irradiated area.

2.3. Characterization

The morphological variations of n-PSi thin films annealed with different Nd:YAG laser pulses (3, 5, 10, and 20) were analyzed using a high-resolution field emission scanning electron microscope (FESEM, NOVA NANO SEM 450) equipped with an energy dispersive X-ray (EDX) detector. The structural properties of the as-prepared n-PSi thin films were characterized by X-ray
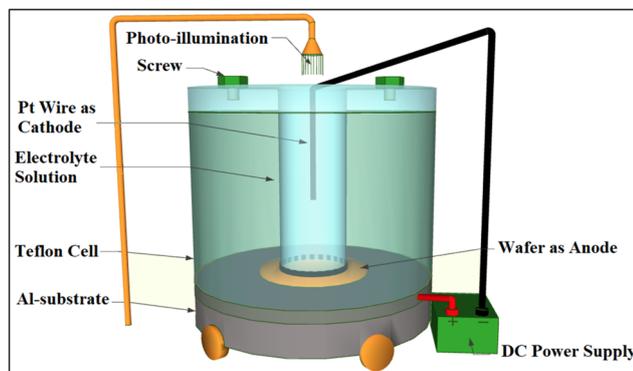
diffraction (XRD) using a PANalytical X'Pert Pro Diffractometer, which operates at 40 kV and 30 mA with Cu-Kα radiation ($\lambda = 1.54056$ Å). The root mean square (RMS) roughness values of the porous layer for different samples were measured using atomic force microscopy (AFM). The optical properties of the thin films were examined through photoluminescence (PL) spectroscopy, recorded using a Jobin Yvon HR 800 UV spectrophotometer equipped with a He–Cd laser ($\lambda = 325$ nm, 20 mW). Electrical characteristics, including current–voltage (I–V) and current–time (I–t) responses of the fabricated MSM-UV photodetectors (MSM-UVPDs), were measured using a Keithley electrometer (model 6517A).

3.   Results and discussion

3.1.   Morphological and structural characteristics

The optimum n-PSi films were prepared at a current density of 45 mA cm^{-2}. The films were annealed under different pulses (3, 5, 10, and 20) of Nd-YAG laser with fluence of 40 mJ cm^{-2}. Contrary to conventional laser untreated n-PSi films, the laser
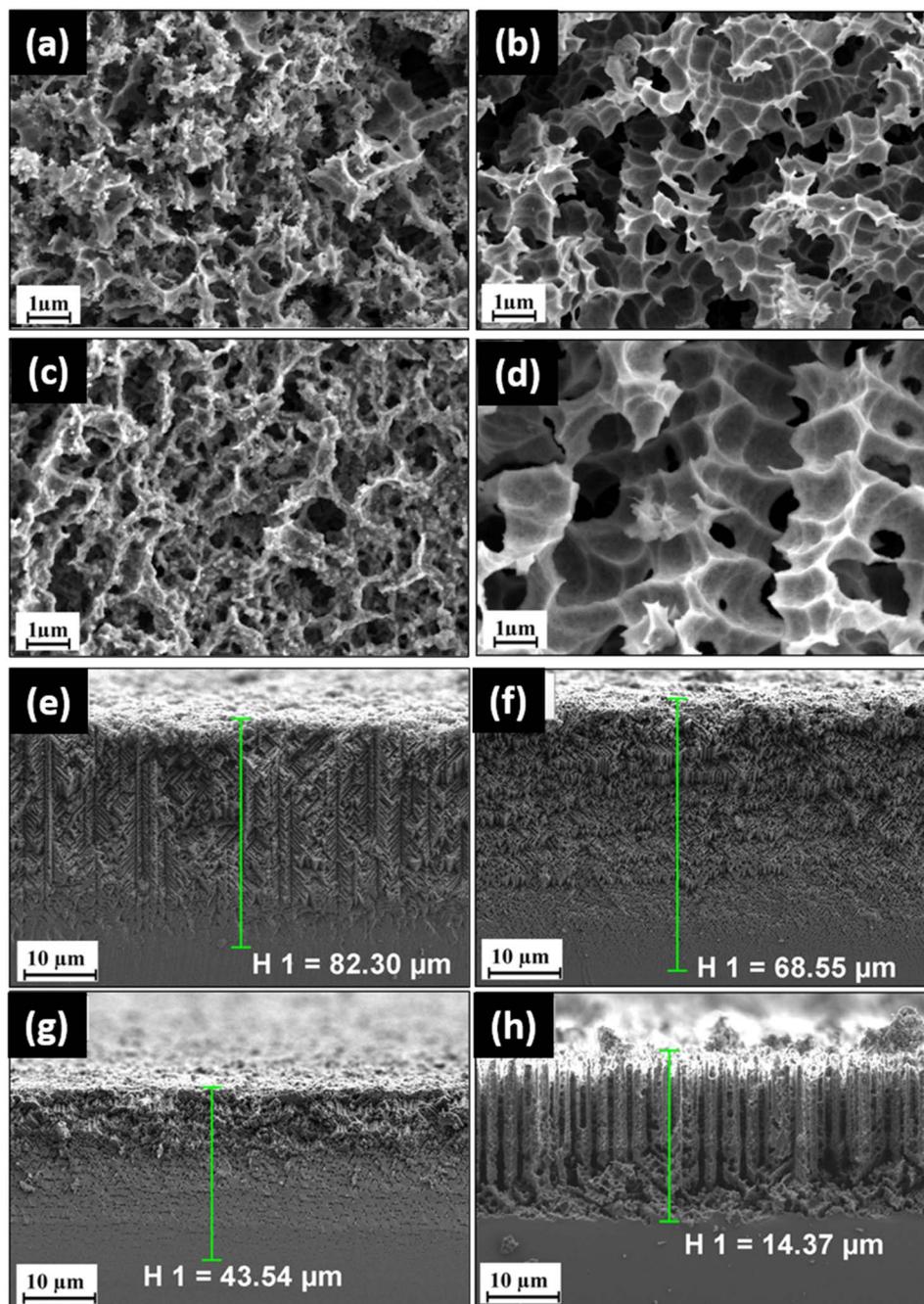

Fig. 3   Top-view FESEM images of the n-PSi after exposure to (a) 3, (b) 5, (c) 10, and (d) 20 laser pulses. The corresponding cross-sectional views of the n-PSi samples after exposure to (e) 3, (f) 5, (g) 10, and (h) 20 laser pulses.

irradiated films are covered with droplet-like Si particles. A possible reason for the formation of droplets is the phase transition *via* explosive crystallization (EC). In this case, the amorphous phase exhibits higher free energy compared to the crystalline phase, thus crystallization occurs with the release of latent heat.[14,15] The n-PSi surface pores appeared to be filled or covered more and more by the Si that is evaporated and condensed after 3 pulses irradiation, Fig. 3(a). The annealing step leads to threshold fluence increase. Increasing the number of laser pulses leads to the formation of more droplets, as shown in Fig. 3(b). The surface of the laser treated n-PSi after an increase in number of pulses to 5 showed that this behaviour was retained. The average pore diameter was estimated using eqn (1). An increase in the pore diameter was observed upon increasing the number of pulses number up to a certain limit, after which the pore diameter began to decrease with further pulse number increase. Morphology evolution as the major difference at higher pulses is associated with hydrogen. The 10-pulses annealed sample (Fig. 3(c)) showed a change in surface morphology, attributable to the local heating by the laser beam, which causes evaporation and re-condensation on the surface. The 20-pulses annealed n-PSi sample (Fig. 3(d)) showed a surface similar to that of 10-pulses obtained surface, only that

the 20 pulses annealed surface pores get increasingly filled and covered by the condensed n-PSi after evaporation with pores size ≈ 2.33 nm (where the larger pores sizes appeared).

In addition, the distribution of majority of the pores was random. The pores are mostly dense, and spherically shaped, while others were elongated, non-uniform, and square-shaped. It is believed that the microstructure and diameter of a pore depend on the conditions of the etching process such as the duration time, HF concentration, current density, and temperature.[16,17] The corresponding cross-sectional images of the n-PSi layers of the samples show spongy, irregular shaped pores with uniform wall thickness. The thicknesses of the n-PSi layers were found to be 14.37, 43.54, 68.55, and 82.30 μm for the samples exposed to 20, 10, 5, and 3 laser pulses, respectively, Fig. 3(e)–(h). EDX elemental analyses of the films are shown in Fig. 4, revealing the presence of Si as the main constituent along with O and F atoms.

Fig. 5 illustrates the XRD patterns of the n-PSi samples after exposure to different laser pulses (3, 5, 10, and 20). The laser-annealed n-PSi samples were found to have higher XRD peak intensities compared to the untreated samples. The intense diffraction peak at $2\theta = 28.42°$ was assigned to the nano-crystallite growth of lattice planes along the (111) plane. The

(a)

Element	Wt%
O	22.5
F	2.7
Si	74.8
Total	100

(b)

Element	Wt%
O	39.7
Si	60.3
Total	100

(c)

Element	Wt%
O	30.5
F	6.9
Si	61.2
Total	100

(d)

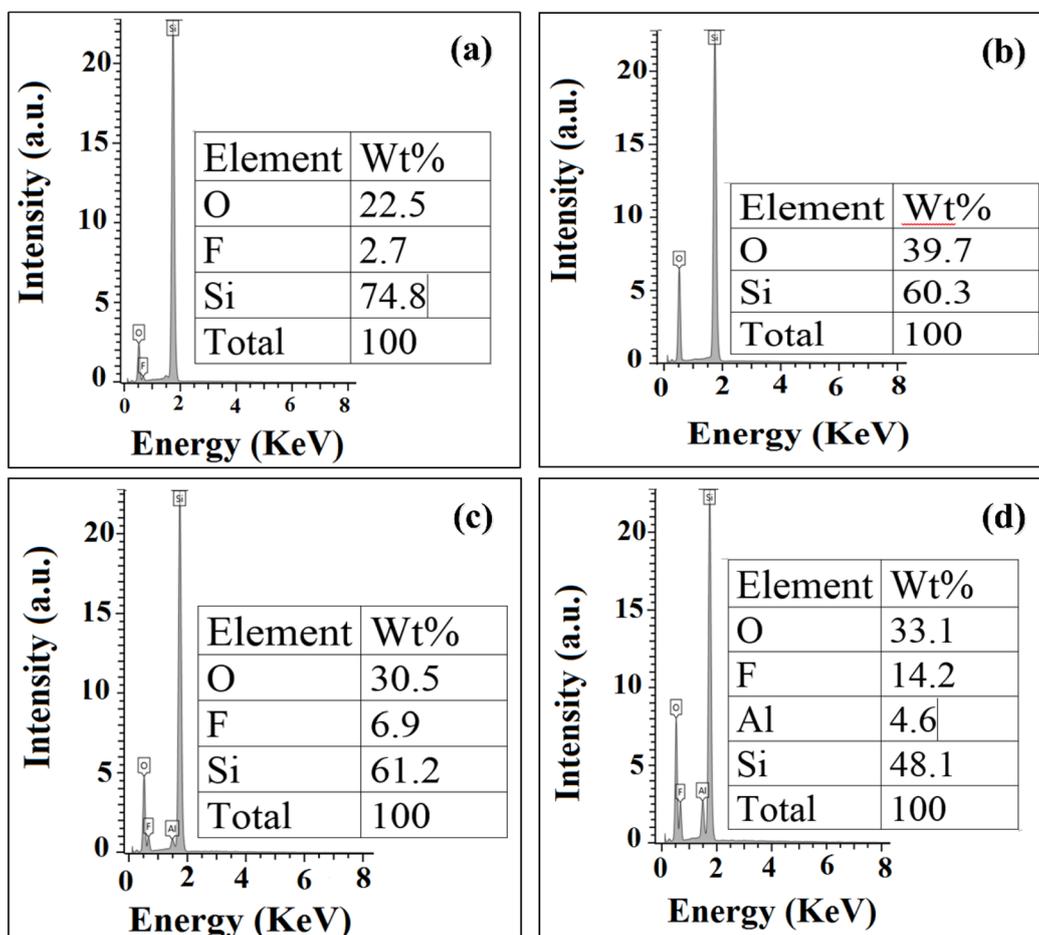| Element	Wt%
O	33.1
F	14.2
Al	4.6
Si	48.1
Total	100

Fig. 4 EDX spectra of the n-PSi films exposed to (a) 3, (b) 5, (c) 10, and (d) 20 laser pulses.
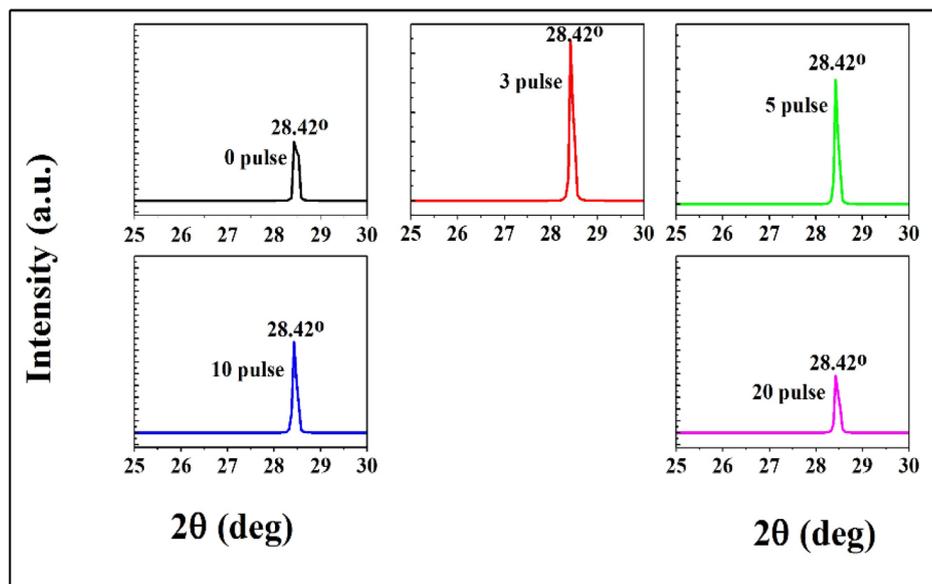
Fig. 5 XRD patterns of the n-PSi samples annealed under varying laser pulses.

crystallite size was calculated using Debye–Scherer equation, see Table 1. The sample exposed to 3 laser pulses showed the largest crystallite size ($\approx$ 87.02 nm). The samples exposed to higher numbers of laser pulses showed approximately uniform average crystallite size. The samples revealed average crystallite sizes of ~63.16 nm, ~58.02 nm, and ~57.98 nm upon exposure to 5, 10, and 20 laser pulses. This is consistent with the sharpness and intensities of the diffraction peaks. The slight decrease in crystallite size can be deduced from the increase in the FWHM. Therefore, the n-PSi (111) layer exposed to 3 laser pulses was selected for use in fabricating the photodetector device. As the number of pulses increases (>3), more energy is absorbed to break the crystals, leading to decrease in crystallite size.

The mismatch between the n-PSi (111) layer and substrate (bulk Si) was investigated based on the average strain ε_{zz} (%). Table 2 presents the values estimated for the average discrepancy ε_{zz} (%) as a function of varying laser pulse number. The observed decrease in ε_{zz} (%) values with increase in the number of laser pulses number can be attributed to growth of nanocrystallites, resulting from free energy minimization and enhanced nucleation. At 3 pulses, the ε_{zz} (%) = −0.90369 is the highest value achieved for the fabricated n-PSi samples, thus considered as the best sample for the MSM UV photodiode fabrication. Furthermore, the positive and negative signs of ε_{zz} (%) indicate compressive and tensile strain occurrence in the nanoporous films. The compressive stress is important in materials with smaller volumes, which leads to columns, shortening of bars, *etc.* inside the structure.[18] Besides, this increase in the stress is possible until the attainment of compressive strength. Conversely, nanocrystallites can be elongated with the application of tensile strain.

Fig. 6(a)–(d) presents the AFM images of the n-PSi samples annealed at varying number of laser pulses of 3, 5, 10, and 20, revealing the formation of rough surface structure with multiple nanosized pores. The 3D AFM image of the laser-treated layer

Table 1 Average crystallite size variation for annealed n-PSi with different laser pulses

Number of pulses	2θ (degree)	FWHM (degree)	Crystallite size (nm)
0	28.4624	0.1556	55.04
3	28.4269	0.0984	87.02
5	28.4624	0.1356	63.16
10	28.4634	0.1476	58.02
20	28.4675	0.1477	57.98

was carried out over a 5 μm × 5 μm dimension. The n-PSi layer exhibits inhomogeneous proportion of large numbers of irregular pillars of silicon and randomly distributed voids over the surface. There was an observed increase in grains' height and surface roughness (R_{rms}) upon increase in the laser's fluence (Table 2). After laser irradiation, a hillock surface (pyramid-like) was also observed. The increase in R_{rms} roughness after laser irradiation is attributable to the porous layer re-melt connected to a rough surface produced by rapid solidification. The process of solidification could create ripples very fast.[19] Furthermore, the analyses of AFM showed that the n-PSi layer overall structure strongly depended upon the irradiating laser flounce. Spacing and pore diameters were varied greatly over a wide

Table 2 Variation of average discrepancy and roughness values of annealed n-PSi at different laser pulses

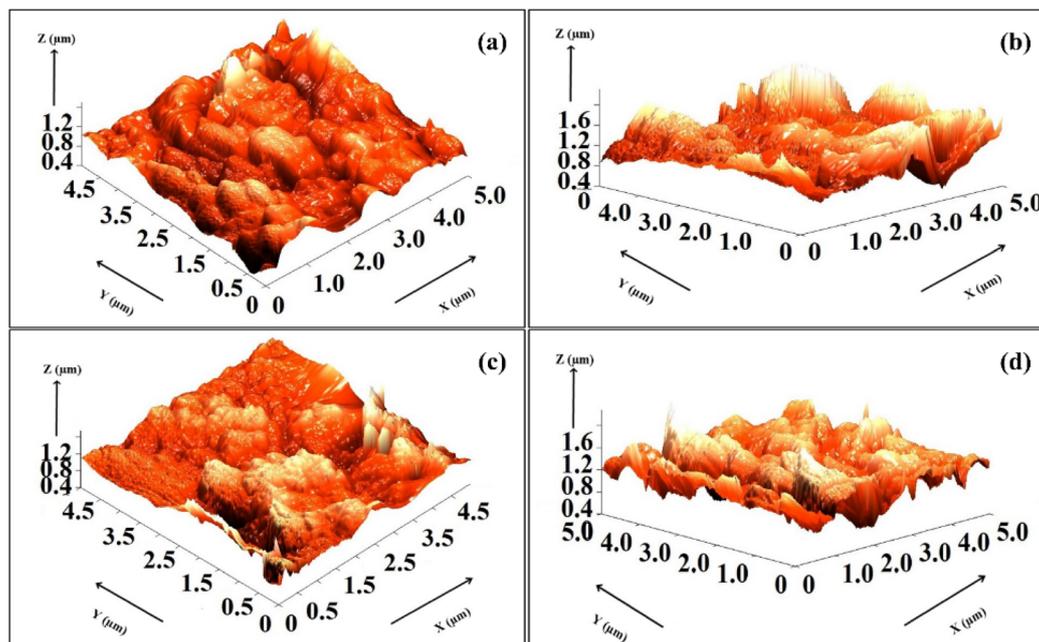| Number of pulses	C_0 (nm)	C (nm)	ε_{zz} (%)	R_{rms} (nm)
3	5.62812	0.542	−0.90369	133
5	6.27178	0.542	−0.91358	150
10	6.27964	0.542	−0.91368	170
20	6.27088	0.542	−0.91356	217

Fig. 6 3D AFM images of the n–PSi samples annealed at (a) 3, (b) 5, (c) 10, and (d) 20 laser pulses.

nanometer scale range with increased surface layer compactness, possibly due to the recrystallization of the top layer.[20] This recrystallization is ascribed to the surface energy reduction.[21] At longer durations the surface becomes rougher. Moreover, at pulse duration of 3, the pore depth and average surface roughness rapidly increased.

3.2. Optical and optoelectronic characteristics

Fig. 7 presents the PL spectra of the laser-annealed n-PSi samples for different laser pulses, revealing a prominent emission peak in the visible region. Upon increasing the number of laser pulses from 3 to 20, continuous visible peak red shift (from 500 to 700 nm) was observed. This longer wavelength shift can be ascribed to the quantum confinement effect weakening of the nanocrystallites,[22] which indicates enhancement in porosity of the sample. PL emission bands in the wavelength range 400–900 nm can be assigned to the S-band.[23] The S-band was observed at 523.43, 633.77, 664.82, and 636.06 nm for the samples treated with 3, 5, 10 and 20 laser pulses, respectively. Furthermore, the intensity of the PL band decreased with increasing the number of pulses, which indicates significant change in the n-PSi porosity, since the intensity of the PL intensity is proportional to the number of photons emitted by the porous surface. The higher energy PL band indicates recombination of surface-state, while the lower one originates from the quantum confinement effect.[24]

Table 3 presents a summary of the change in average pore diameter and optical band gap energy of the n-PSi films upon exposure to different number of laser pulses. Based on the model of quantum confinement, the shorter wavelength PL peak signifies more confinement strength and thus wider band gap energy.[25] The wider band gap energy of 2.36 eV for the n-PSi
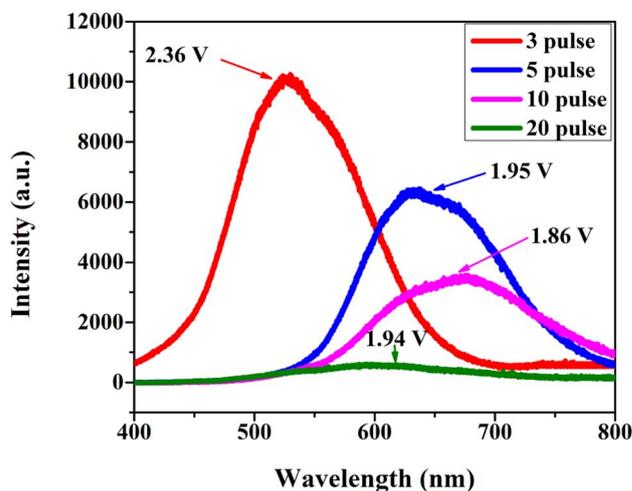

Fig. 7 PL spectra of the n-PSi films annealed at different number of laser pulses.

sample exposed to 3 laser pulses confirms stronger size confinement. However, as the number of laser pulses increased, weaker confinement was recorded (lower band gap of 1.86 eV). This effect of de-confinement is a clear indication of porosity enhancement and bigger nanocrystallites formation due to melting-assisted laser effect. The electron–hole (e^{-}–h^{+}) recombination probability became higher in this situation, in the nanoporous structures, which led to quantum efficiency enhancement. Table 4 gives a comparison between the obtained crystalline size, band gap energy and pore diameter to those reported in the literature for n-PSi.

The observed change in band gap of the prepared PSi upon laser annealing (Table 3) can be attributed to alterations in pore

Table 3 The energy gap and the average pore diameter of the n-PSi grown at different laser pulses

Number of pulses	Energy gap (eV)	Average pore diameter (nm)
3	2.36	2.17
5	1.95	2.26
10	1.86	2.31
20	1.94	2.33

Table 4 Comparison of the crystallite size, band gap energy, and pore diameter of the n-PSi obtained in the present study with other similar reported works in the literature

Crystallite size (nm)	Energy gap (eV)	Pore diameter (nm)	References
87.02	2.36	2.17	Present work
4.27	1.65	—	26
54.64	1.99	20.77	27
55	1.95	77	28
18.09	1.88	—	29

size, surface roughness, oxidation and doping.[30] Initially, etching introduces surface roughness to the porous silicon, which can result in a decrease in the band gap due to the creation of surface states. However, the smaller pores produced by the etching process can lead to a larger band gap due to quantum confinement effects. Etching also exposes the PSi to oxygen, leading to oxidation and the formation of a silicon oxide layer, which can increase the bandgap due to the creation of a wider band gap oxide layer. Laser annealing then transformed the morphology of the PSi, where the local heating by the laser beam causes evaporation and re-condensation on the surface.[31–33] This leads to the reduction and filling of the surface pores by the condensed n-PSi material after evaporation. This explains the decrease in the energy gap with increasing the number of laser pulses. The laser-induced changes are

dependent on the conditions and properties of the PSi itself. The structure shown in Fig. 8 depicts a planar photo-conductive detector based on the common metal–semiconductor–metal (MSM) configuration.

Fig. 9 shows the *I–V* characteristics of the fabricated MSM photodetectors based on the n-PSi films annealed at different number of laser pulses. The current was recorded under dark and UV light (wavelength of 380 nm and intensity of 1.5 mW cm^{-2}) in the voltage range from +5 V to −5 V. The graphs show Schottky *I–V* characteristics for both forward and reverse bias and was the best for the n-PSi sample annealed with 3 laser pulses. For all designed photodiodes, the measured hysteresis loop under the forward bias was ascribed to the sluggish capture centres generated by holes.[34] Nevertheless, under reverse bias, the hysteresis loop was absent, in agreement with the literature.[35] The attained *I–V* behavior was similar to the one observed for Si based p–n junction but with a lower slope. Note that the Pt/n-PSi/Pt structure comprised of two junctions linked in series; the Pt/n-PSi Schottky barrier with high resistance of porous Si film and the PSi/Si heterojunction. Existence of these contacts aided the bias to change between −5 V and +5 V. The observed enhancement in the photodetector's forward current was attributed to the reduction of resistivity in the porous structure, which can be ascribed to the enhancement in crystallinity of the porous film upon laser annealing. Exposure with high laser flounce (40 mJ cm^{-2}) could enhance the resistivity of the porous film by generating large number of defects in the laser exposed area including recombination or trap centres with deeper energy states in the forbidden energy gap of the PSi film.[36] Generally, the *I–V* characteristics of the fabricated photodetectors were improved with the number of laser pulses, indicating some positive influence on the photodetector's performance.

Fig. 10 illustrates the spectral sensitivity of the designed MSM n-PSi photodetectors under different bias voltages (+3, +5, and +7 V applied for 20 s intervals). The dynamic response of these photodetectors showed rectangular behaviour, where the photocurrent values for each *on/off* phase were stable and repeatable. In
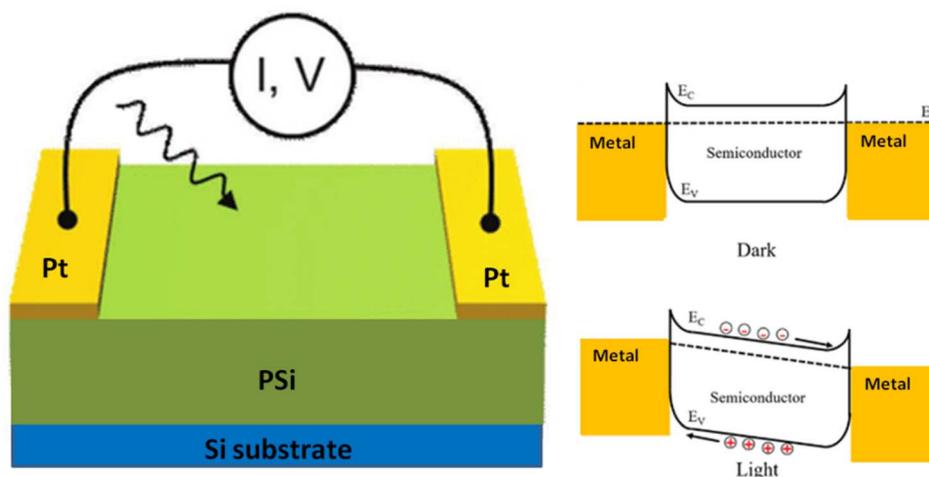

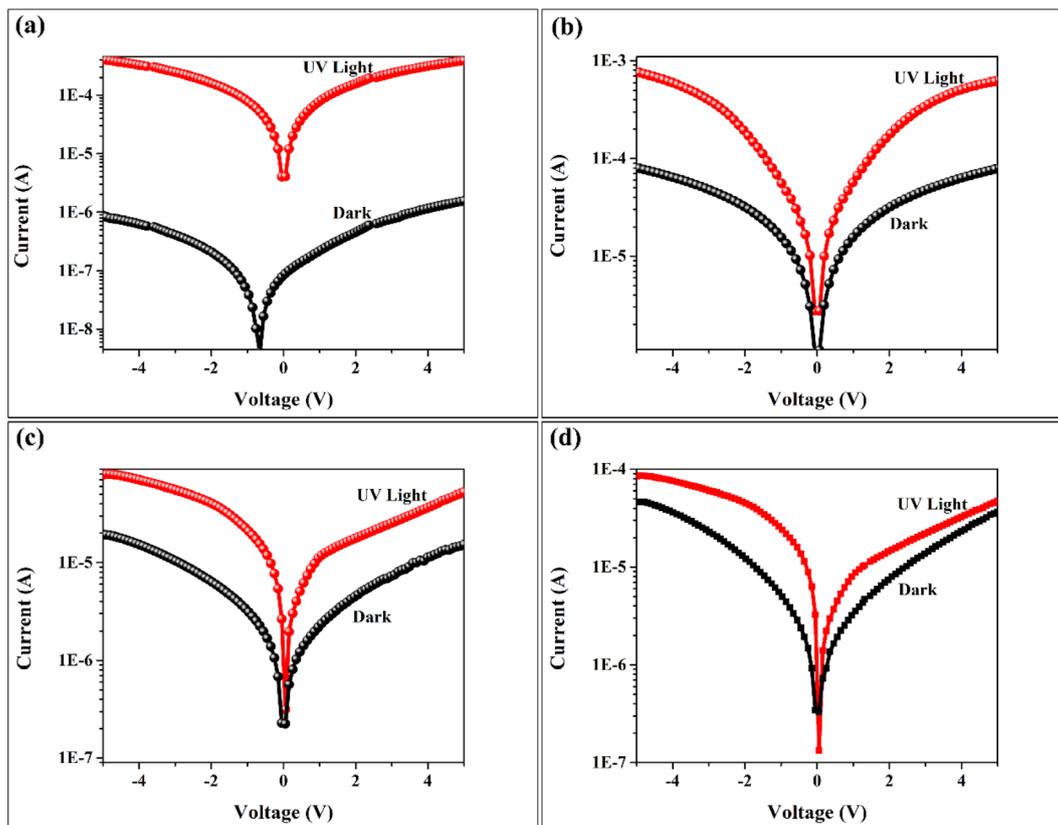**Fig. 8** Energy bandgap diagram of the Pt/PSi/Pt device.

Fig. 9 $I-V$ characteristics of the designed photodetectors based on n-PSi films annealed at (a) 3, (b) 5, (c) 10, and (d) 20 laser pulses recorded under dark and UV light conditions.

Fig. 9(a) and (c), the photocurrent values increase as a function of bias. However, in Fig. 9(b) and (d), the photocurrent is maximum for 5 V compared to 7 V. The photocurrent in PSi is influenced by the separation and recombination of charge carriers (e–h). The bias voltage can affect separation efficiency, leading to changes in photocurrent.[37] Bias voltage also influences the recombination centers and occupation of trap states formed by the defects in PSi, affecting photocurrent. As earlier explained, the band gap energy of 2.36 eV recorded for 3 laser pulses reduced to 1.86 eV as the number of laser pulses increased, due to weaker quantum confinement. This effect of de-confinement is indicative of enhanced porosity and larger nanocrystallites due to melting-assisted laser effect. Thus, for samples annealed with 3 laser pulses, the strong confinement allows for improved generation and separation of charge carriers as the bias voltage is increased. In contrast, the de-confinement or weaker quantum confinement of the PSi samples annealed with 20 pulses lowers the efficiency of charge generation and separation as bias voltage is increased. Regardless of the laser annealing procedure and applied voltage, the present photodetectors displayed good stability and repeatability characteristics.

In addition, the recovery and rise times of the fabricated photodetectors, estimated from the current–time response, were found to be very rapid. The Φ_B for the photodetector made from the 3-pulses- annealed n-PSi film is 0.95 eV. The Φ_B was found to depend on the number of laser pulses used for the annealing of the n-PSi films, which can be attributed to the varied roughness of the surface layers. Consequently, the n-PSi/ Pt interface is notably altered, enhancing the electrical properties of the photodetector.[38] The current response was used to calculate the percentage photosensitivity ($S\%$) of the MSM photodetector (eqn (5)). The sensitivity of the photodetectors made from the laser-annealed n-PSi films is much higher than that made from laser untreated film. Moreover, the time of response and recovery of the photodetector made from the n-PSi film annealed under 3 laser pulses are 0.29 s and 0.44 s, respectively. These values are the shortest for the laser annealed n-PSi- based photodetectors with better performance than those reported in the literature.[38,39] This observed swift response can be ascribed to the laser annealed (at 3 pulses) n-PSi samples without defects and high quality with large photoactive surface area. On contrary, the sluggish response of the device fabricated using films annealed with higher number of laser pulses can be ascribed to the existence of grain boundaries and increased oxygen adsorption at the wide surface layer.[40]

Following the theory of thermionic emission-diffusion,[41,42] the values of Schottky barrier height (Φ_B) and the ideality factor (n) were estimated *via*:

$$I = I_0 \exp\left(\frac{qV}{nkT}\right)\left[1 - \exp\frac{-qV}{kT}\right] \quad (3)$$
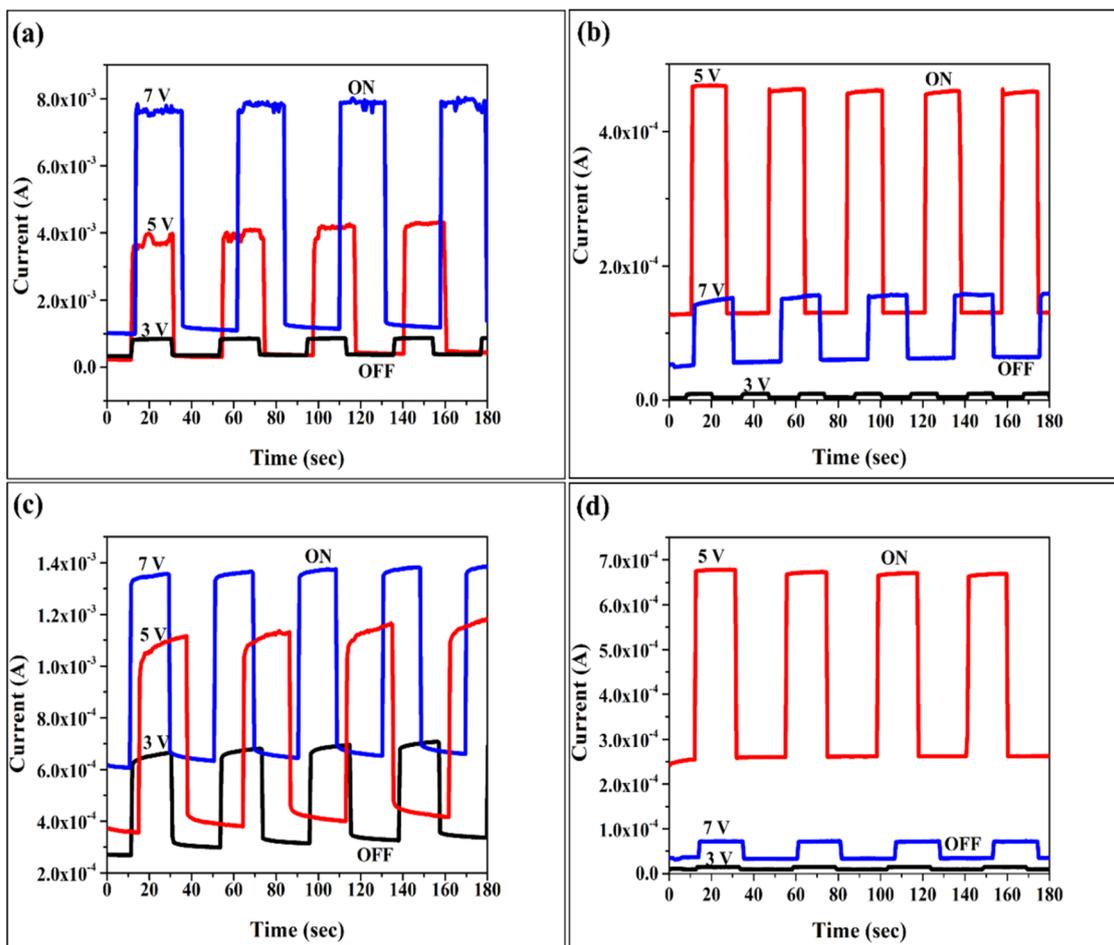
Fig. 10 Response–relaxation behavior of the MSM photodetectors as a function of applied bias under UV light exposure recorded at each on/off cycle for the films annealed under (a) 3, (b) 5, (c) 10, and (d) 20 laser pulses.

$$I_0 = AR^*T^2 \exp\left[\frac{-\Phi_B}{kT}\right] \quad (4)$$

where I_0 presents the saturation current, T represents the temperature, k denotes the Boltzmann constant, R^* (≈ 112 A cm^{-2} K^2) signifies the effective Richardson coefficient, A refers the Schottky contact area (≈ 0.25 cm^2), and q is the charge of electron.

The intercept of ln I versus V plot was used to determine Φ_B. Eqn (4) was used to find the value of I_0 for different current densities. The value of Φ_B for the fabricated photodetector obtained with 45 mA cm^{-2} was 0.73 eV. The slight changes in the Φ_B values for various current densities can be due to the varied surface roughness of the samples, which significantly affected the n-PSi/Pt interface, leading to improvement in the electrical features.[43] The observed enhancement in the value of Φ_B for samples prepared at high current density was ascribed to the existence of high-level porosity, which could shift the Fermi level towards the valence band and diminish the dark current. The enhancement in ideality factor can be attributed to the occurrence of large number of interface states.[44] It was shown that the existence of 2 hetero-junctions in the samples such as

at the interface of substrate and n-PSi and inside the n-PSi and Pt border was mainly responsible for such improvement.[40,42] Besides, the inhomogeneity of barrier heights might have made n large, as acknowledged by a related study.[45] The current *versus* time variation was used to evaluate the photodetector's sensitivity (S) by the relation:[46]

$$S\,(\%) = \frac{I_{ph} - I_d}{I_d} \times 100 \quad (5)$$

where I_{ph} and I_d are the of photo- and dark-density current, respectively.

The measured photocurrent of the n-PSi specimen grown at varied current density revealed high stability and repeatability during each on/off cycle. Both the response and recovery time for n-PSi structure grown at 45 mA cm^{-2} was found to be 0.47 s and 0.47 s, respectively. These achieved times are the shortest compared to those reported in the literature.[47,48] The observed rapid response at utmost current density was ascribed to the defects-free nature, high quality and, enlarged area of the photoactive surface of the prepared n-PSi layer. Furthermore, the prompt response of the photodetector was linked to the short transit time of the photo-generated carriers characterized

by their long lifetime.[47,48] On the contrary, the sluggish response of the photodetector is attributable to the existence of grain boundaries and increase in the oxygen adsorption on the wide surface.[40]

The obtained photodetector's performance was assessed *via* responsivity (R, in A W^{-1}) which was expressed as the device photocurrent to the incident optical power[48] ratio given by:

$$R = \frac{I_{ph}}{P_{inc}} = \frac{I_{ph}}{E \times A} \tag{6}$$

where E denotes the incident photon energy recorded by a standard UV power-meter (Newport power meter, Model 2936-C, USA). The responsivity of the studied photodetector in the wavelength region of 300–900 nm was recorded at room temperature under the optimum bias voltage of +5 V.

Fig. 11 shows the photo-response of the fabricated photodetectors made of the laser annealed n-PSi films as indicated by peak values (λ_P and R_P). Regardless of the number of laser pulses, the responsivity behavior showed a significant visible peak centred at 380 nm, which arose from light absorption in the depletion region of n-PSi. The maximum responsivity at 380 nm can be attributed to a combination of quantum confinement effects, defects, and optical properties (optical absorption, scattering and reflection).[49,50] The 380 nm wavelength corresponds to the optimal bandgap energy for PSi structure, leading to enhanced absorption and reduced recombination losses. The valence band edge in PSi is

responsible for the responsivity at 380 nm. The quantum confinement leads to increase in bandgap energy, which results in a blue shift, making PSi more responsive to UV light. The increase in bandgap energy also enhances UV absorption. Clearly, the responsivity was enhanced upon the laser annealing of the porous films. The 3-pulses-based photodetector showed a maximum R_P of 2.01 A W^{-1} and found to be superior compared to the reported values in the literature.[38,51] The high surface-to-volume ratio of PSi due to the etching process leads to a large number of surface states and defects. However, the photoexcited carriers in the UV region have sufficient energy to overcome the recombination centers generated by the defects, resulting in a higher photoresponse. Additionally, the appearance of small shift in the peak value (from 380.07 to 380.21) can be ascribed to the morphological and structural changes of the n-PSi film. It was asserted that the lifetime of the generated additional carriers, which is a significant factor in the fabrication of photodetector, could be improved by laser annealing. Table 5 depicts the characteristic parameters of the fabricated photodetectors. Evidently, the photodetector obtained using n-PSi layer with 3 laser pulses treatment displayed the best performance. In Table 5, the barrier height is observed to decrease with increasing the bias voltage. When a forward bias voltage is applied, the barrier height is reduced, allowing more current to flow across the junction. When the bias voltage is applied, an electric field is created and thermal emission (Schottky effect) is increased across the metal–semiconductor
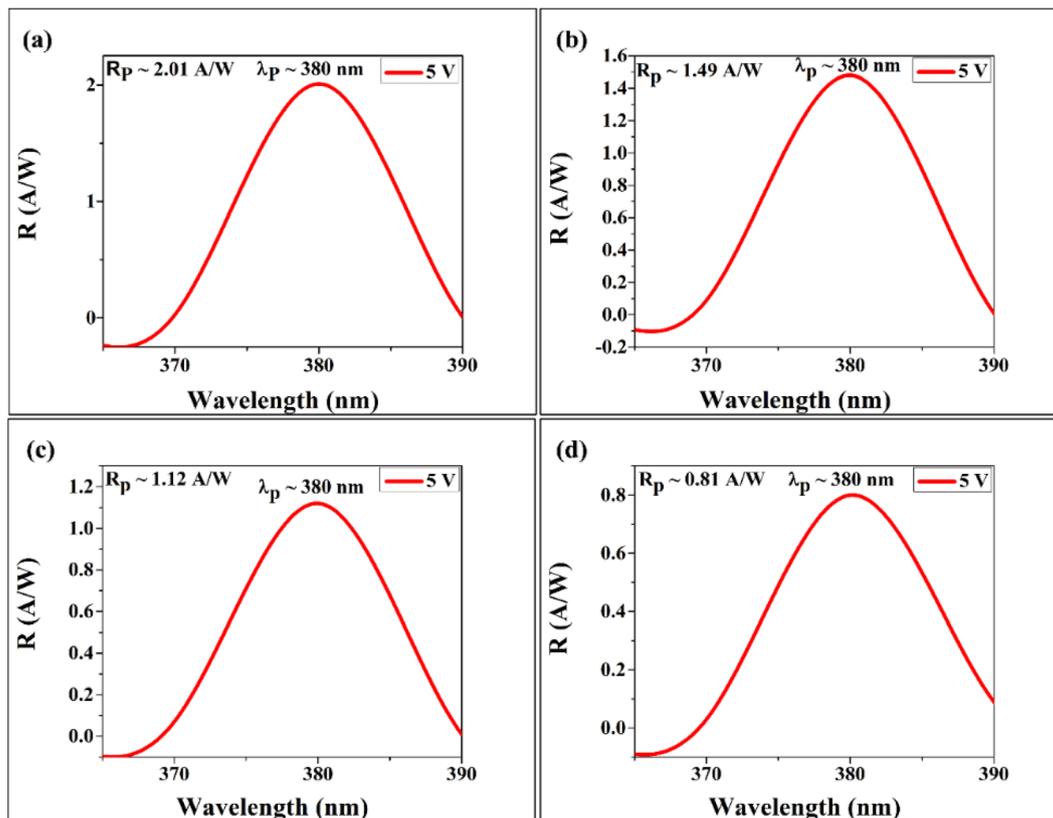

Fig. 11 Responsivity of the fabricated photodetectors made of n-PSi films annealed under (a) 3, (b) 5, (c) 10, and (d) at 20 laser pulses recorded at applied voltage of +5 V.

Table 5 Calculated parameters of the designed photodetectors obtained at changing laser pulses and exposed to UV light (380 nm)

Pulses	V_{bias} (V)	I_d (A)	I_{ph} (A)	S (%)	G	R (A W^{-1})	Φ_B (eV)	I_o (A)	t_{Res} (s)	t_{Rec} (s)
3	3	3.90×10^{-4}	8.68×10^{-4}	122.56	2.22	2.01	0.95	1.11×10^{-7}	0.46	0.48
	5	3.90×10^{-4}	4.1×10^{-3}	951.28	10.51				0.29	0.44
	7	1×10^{-3}	7×10^{-3}	600	7.0				0.45	0.49
5	3	6.43×10^{-6}	8.92×10^{-6}	38.72	1.38	1.49	0.93	2.26×10^{-6}	0.47	0.41
	5	1.29×10^{-4}	4.66×10^{-4}	261.24	3.61				0.45	0.41
	7	1.58×10^{-4}	5.92×10^{-4}	274.68	3.74				0.68	0.47
10	3	3.12×10^{-4}	6.64×10^{-4}	112.82	2.12	1.12	0.92	3.05×10^{-7}	0.44	0.48
	5	4.26×10^{-4}	11×10^{-4}	158.21	2.58				0.45	0.43
	7	6.62×10^{-4}	13×10^{-4}	96.37	1.96				0.98	0.52
20	3	1.16×10^{-5}	2.11×10^{-5}	81.89	1.81	0.81	0.88	1.52×10^{-8}	0.49	0.48
	5	2.57×10^{-4}	6.82×10^{-4}	165.36	2.65				0.48	0.47
	7	3.05×10^{-5}	7.58×10^{-5}	148.52	2.48				0.50	0.48

Table 6 Comparison of the responsivity of the fabricated photodetectors with others reported in the literature

Si-based device structure	Wavelength (nm)	Bias voltage (V)	Responsivity (A W^{-1})	Ref.
Pt/n-PSi/Pt	380	5	2.01	Present work
Au NPs/PSi	365	10	0.2	23
Visible-blind ultraviolet photodetectors on porous silicon carbide substrates (PSiC)	350	5	0.06	54
Al/PSi/Si/Al (Al/porous silicon/crystalline silicon/Al structure)	365	5	0.5	38
Au:CuO nanocomposite/PSi	365	2	0.75	28

interface. The electric field and increased thermal emission then induces charges in the metal electrode, which reduces the barrier height. Table 6 compares the responsivity of the best photodetector prepared in this study with those reported in literature, which clearly showed the outperforming nature of our photodetector. This aligns with Ahmed et al.,[52] who modified Si structures into PSi via anisotropic electrochemical etching for optoelectronic applications, yielding ~250 nm pores and a direct energy gap of 1.73 eV with 11.18% sensitivity at 786 nm. Similarly, Ahmed et al.[53] anodized n-type monocrystalline Si in an ethanoic-HF solution, producing ~700 nm pores, a 1.80 eV direct bandgap, and 9.4% sensitivity at 785 nm. However, our study reports a significantly higher sensitivity of 951.28%, highlighting a major distinction.

4. Conclusion

Nanoporous silicon (n-PSi) films were grown via optimized photoelectrochemical etching of Si wafers. The grown n-PSi films were irradiated with different Q-switched Nd:YAG laser pulses (3, 5, 10 and 20) at fixed wavelength of 1068 nm, varied pulse durations of 3–20 ns, and constant repetition rate of 10 Hz. The n-PSi sample subjected to 3 laser pulses exhibited the most crystallized surface and largest crystallite size (≈ 87.02 nm), and was thus selected for the fabrication of Pt/n-PSi/Pt photodetector. The Pt/n-PSi/Pt UV photodetector demonstrated improved detection efficiency and enhanced electrical response. The UV photodetector displayed good I–V characteristics, resulting in higher photosensitivity (951.28) and responsivity (2.01 A W^{-1}), and faster recovery time (0.48 s) and response time (0.44 s) compared to known photodetectors. The proposed technique may constitute a basis for controlled tuning of various nanomaterials with desirable properties for high performance nanodevices applications.

Data availability

The data supporting this article are included in the manuscript.

Conflicts of interest

The authors declare that they have no conflict of interest.

Acknowledgements

References

1 A. A. Thahe, et al., Opt. Quantum Electron., 2020, 52, 1–18.

2 S. B. Khan, et al., Materials, 2019, 12, 1483.

3 N. Naderi and M. Hashim, Int. J. Electrochem. Sci., 2012, 7, 11512–11518.

4 O. S. Shafeq, et al., Nickel Oxide Thin Films Grooved by Laser Processing, IOP Conf. Ser.: Mater. Sci. Eng., 2020, 072016.

5 A. A. Thahe, et al., Solid-State Electron., 2020, 171, 107821.

6 S. Ueamanapong, et al., Adv. Sci. Lett., 2013, 19, 997–1000.

7 A. A. Thahe, *et al.*, *Nanoscale Adv.*, 2025, **7**, 1627–1635.

8 H. Cao, *et al.*, *J. Mater. Res. Technol.*, 2025, **35**, 809–835.

9 J. Dian, *et al.*, *Appl. Surf. Sci.*, 2004, **238**, 169–174.

10 A. A. Thahe, *et al.*, *Opt. Mater.*, 2018, **84**, 830–842.

11 S. Yae, *et al.*, *Sol. Energy*, 2006, **80**, 701–706.

12 S. E. El-Zohary, *et al.*, *J. Nanomater.*, 2013, **2013**, 568175.

13 A. A. Thahe, *et al.*, *Mater. Res. Express*, 2017, **4**, 116203.

14 C. Li and P. Miao, *Appl. Phys. Lett.*, 2025, **126**, 043701.

15 A. A. Thahe, *et al.*, *Optik*, 2018, **168**, 424–431.

16 S. A. Razek, *et al.*, *J. Appl. Phys.*, 2014, **115**, 194305.

17 A. M. Mohamed, *et al.*, Recent advances in the use of silicon-based photocathodes for solar fuel production, *Advances in Silicon Solar Cells*, Springer, Cham, 2018, 229–267, DOI: **10.1007/978-3-319-69703-1_9**.

18 A. A. Saleh, *et al.*, *Int. J. Hydrogen Energy*, 2019, **44**, 24418–24429.

19 J. D. Majumdar and I. Manna, *Sadhana*, 2003, **28**, 495–562.

20 M. Hajji, *et al.*, *Thin Solid Films*, 2006, **511**, 235–237.

21 V. Lysenko and S. Volz, *Phys. Status Solidi A*, 2000, **182**, R6–R7.

22 R. Prabakaran and R. Kesavamoorthy, *Bull. Mater. Sci.*, 2005, **28**, 219–225.

23 R. A. Ismail, *et al.*, *Appl. Nanosci.*, 2017, **7**, 9–15.

24 C. Chen and Y. Chen, *Solid State Commun.*, 1999, **111**, 681–685.

25 K. Cheah, *et al.*, *Appl. Phys. Lett.*, 1993, **63**, 3464–3466.

26 N. M. Ahmed, *et al.*, *Procedia Eng.*, 2013, **53**, 393–399.

27 R. Radzali, *et al.*, *AIP Conf. Proc.*, 2017, 020003.

28 H. H. Rashed and J. Moatasemballah, *Al-Nahrain J. Sci.*, 2017, **20**, 49–59.

29 D. Alima, *et al.*, *J. Appl. Phys.*, 2012, **112**, 114312.

30 M. Xin, *et al.*, *Weld. World*, 2024, **68**, 3033–3050.

31 S. Xiong, *et al.*, *Anal. Chim. Acta*, 2025, **1336**, 343496.

32 X. Li, *et al.*, *Opto-Electron. Adv.*, 2024, **7**, 240085.

33 Y. Zhou, *et al.*, *J. Mater. Res. Technol.*, 2024, **33**, 6084–6089.

34 K. M. A. Saron, *et al.*, *RSC Adv.*, 2020, **10**, 33526–33533.

35 M. A. Qaeed, *et al.*, *ACS Appl. Mater. Interfaces*, 2014, **6**, 9925–9931.

36 S. M. Fawzy, *et al.*, *Sci. Rep.*, 2021, **11**, 13635.

37 R. A. Ismail, *e-J. Surf. Sci. Nanotechnol.*, 2010, **8**, 388–391.

38 R. A. Ismail and M. K. Abood, *Int. Nano Lett.*, 2013, **3**, 11.

39 K. K. Al-Khazraji, *et al.*, *Procedia Eng.*, 2012, **38**, 1381–1390.

40 A. Chouket, *et al.*, *J. Appl. Phys.*, 2013, **114**, 243105.

41 A. A. Rahim, *et al.*, *Phys. B*, 2011, **406**, 1034–1037.

42 M. T. Al-Helaly, *et al.*, *AIP Conf. Proc.*, 2023, **2414**, 030020.

43 J. Perez, *et al.*, *Appl. Phys. Lett.*, 1992, **61**, 563–565.

44 D. Dimova-Malinovska and M. Nikolaeva, *Vacuum*, 2002, **69**, 227–231.

45 K. M. A. Saron, *et al.*, *Appl. Phys. Lett.*, 2021, **118**, 023902.

46 A. M. Selman and Z. Hassan, *Sens. Actuators, A*, 2015, **221**, 15–21.

47 N. M. Ahmed, *et al.*, *AIP Conf. Proc.*, 2012, 196–210.

48 A. B. Taha, *et al.*, *AIP Conf. Proc.*, 2023, 2977.

49 Y. Lv, *et al.*, *Chem. Eng. J.*, 2024, **488**, 151053.

50 L. Guo, *et al.*, *Sens. Actuators, B*, 2012, **166**, 12–16.

51 R. A. Talib, *et al.*, *Mater. Chem. Phys.*, 2016, **181**, 7–11.

52 S. Ahmed, *et al.*, *J. Mater. Sci.: Mater. Electron.*, 2023, **34**, 755.

53 S. Ahmed, *et al.*, *Europhys. Lett.*, 2022, **139**, 36001.

54 N. Naderi and M. Hashim, *Mater. Res. Bull.*, 2013, **48**, 2406–2408.